EES Solar

PAPER

View Article Online
View Journal

Cite this: DOI: 10.1039/d5el00179j

Operando spectroscopic ellipsometry enables direct quantification of dynamic degradation rates in photoelectrochemical cells

Jiri Kollmann, [a] Mauricio Schieda, *[a] Ragle Raudsepp, [a] Sehun Seo, [a] Thomas Klassen [bc] and Francesca M. Toma *[acde]

The instability of photoelectrodes remains a critical barrier to the practical implementation of photoelectrochemical (PEC) systems for solar fuel production. A comprehensive understanding of photocorrosion mechanisms under operating conditions is essential yet challenging to achieve due to the difficulty of real-time, spatially resolved monitoring. In this study, we introduce an *operando*-spectroscopic ellipsometry (SE)-based method for the real-time, quantitative analysis of photoelectrode surface degradation. Using atomic layer deposited TiO_2 thin films with different crystalline phases as model systems, we demonstrate continuous monitoring of degradation rates under *operando* conditions across acidic, alkaline, and near-neutral pH environments, both with and without illumination. PEC *operando*-SE reveals that photocorrosion dynamics are strongly influenced by crystallinity, illumination, and electrolyte conditions. Notably, under illumination, degradation rates vary significantly with TiO_2 crystallinity; slower charge transport in amorphous films accelerates photocorrosion compared to crystalline counterparts. When combined with complementary techniques such as electrochemical impedance spectroscopy, *operando*-SE offers synergistic insights into surface degradation mechanisms and holds strong potential for guiding the development of more stable PEC materials.

Received 24th October 2025
Accepted 3rd March 2026

DOI: 10.1039/d5el00179j

rsc.li/EESSolar

Broader context

Converting sunlight into clean fuels offers a sustainable way to meet the world's growing energy needs while reducing carbon emissions. However, the materials that enable these solar-to-fuel reactions often degrade during operation, limiting their long-term stability. Understanding how this degradation happens is crucial for developing durable photoelectrochemical systems for solar fuel production, yet real-time monitoring across the entire electrode surface has remained a major challenge. In this work, we introduce an *operando* spectroscopic ellipsometry method that allows direct, real-time analysis of photoelectrode corrosion with sub-nanometer precision. Using titanium dioxide films as model systems, we show how crystal structure, light exposure, and electrolyte environment influence their stability. This approach provides clear insight into photocorrosion processes and offers a powerful tool for designing next-generation, long-lasting materials for solar-driven fuel production.

Introduction

To meet the increasing energy needs of our population while respecting our environment, the search for alternative and sustainable energy sources is inevitable. Photoelectrochemical (PEC) cells have attracted the broad attention of the research community in the last decades, as they enable sunlight-driven water splitting to produce green hydrogen and to reduce of CO_2 to hydrocarbons and solar fuels.[1–4] Despite these promising capabilities, limited long-term stability remains the most critical factor delaying the practical commercialization of PEC technologies.[5] Various causes of PEC instability have been identified, including photocorrosion due to self-oxidation or reduction by photo-generated charges, thermodynamic instability in electrolytes, and the degradation of protective layers or co-catalysts.[6–13] These degradation processes primarily occur at the interface between the photoelectrode and the electrolyte.[14,15] Therefore, understanding the phenomena at the interface between the electrolyte and the photoelectrode is important, making real-time monitoring of interface corrosion essential to elucidate degradation mechanisms in PEC systems.

[a]*Institute of Functional Materials for Sustainability, Helmholtz-Zentrum Hereon GmbH, Kantstr. 55, Teltow 14513, Germany. E-mail: mauricio.schieda@hereon.de; francesca.toma@hereon.de*

[b]*Institute of Hydrogen Technology, Helmholtz-Zentrum Hereon GmbH, Max-Planck-Str. 1, Geesthacht 21502, Germany*

[c]*Faculty of Mechanical and Civil Engineering, Helmut-Schmidt-University, Holstenhofweg 85, Hamburg 22043, Germany*

[d]*Chemical Sciences Division, Lawrence Berkeley National Laboratory, 1 Cyclotron Road, 94720, Berkeley 94720, California, USA*

[e]*Liquid Sunlight Alliance, Lawrence Berkeley National Laboratory, 1 Cyclotron Road, 94720, Berkeley 94720, California, USA*

To date, a variety of analytical techniques have been developed to study corrosion in photoelectrodes. PEC-based *in-situ* inductively coupled plasma mass spectrometry,[10,16] for example, enables the detection of dissolved species originating from surface corrosion. Surface-sensitive methods like X-ray photoelectron spectroscopy[17,18] and X-ray absorption spectroscopy[19,20] provide chemical-state information at the electrode interface, thereby enabling indirect interpretation of corrosion mechanisms and performance losses.

Yet, these methods have inherent limitations in capturing the structural and morphological changes at the photoelectrode surface. Direct observation of morphological degradation is typically carried out using scanning electron microscopy and transmission electron microscopy by comparing electrode surfaces before and after operation.[21,22] However, these techniques generally cannot track the real-time progression or pathway of corrosion, as they only provide static snapshots of the surface before and after exposure in the PEC system. For *operando* studies, atomic force microscopy (AFM) has been applied to monitor localized corrosion in real time.[23] However, its application is limited by the small scanning area (a few tens of micrometers), which cannot reflect the whole electrode area. Consequently, there is a clear need for analytical approaches capable of comprehensive analysis of large-area, real-time physical degradation of photoelectrodes under operating conditions.

Spectroscopic ellipsometry (SE) is a powerful, non-destructive technique capable of accurately measuring physical degradation on photoelectrode surfaces across a wide area. It provides direct and highly precise measurements of thin film thickness changes with sub-nanometer resolution.[24–26] It works by analyzing changes in optical polarization, particularly in the complex reflectance ratio, when light is reflected or transmitted through a material. This method allows for the extraction of the key parameters such as optoelectronic properties of the material, thickness, and microstructure. Until now, ellipsometry has primarily been applied to *ex-situ* measurements, which compare the state of the electrode surface before and after operation.[27–30] These measurements offer only averaged information on degradation over the total operation time. Thus, to capture the dynamic changes in materials and interfaces under realistic photoelectrochemical conditions, there is a need for a system that enables real-time tracking of photoelectrode surface degradation using *operando*-SE.

In this study, we present the first application of PEC *operando*-SE to investigate the dynamic degradation of photoelectrodes under PEC operating conditions. This non-destructive technique enables real-time monitoring of physical corrosion at the electrode–electrolyte interface with sub-nanometer resolution. In addition, by integrating SE with electrochemical impedance spectroscopy (EIS), which captures changes in interfacial charge transport and resistance, we provide a comprehensive understanding of how physical degradation correlates with electrochemical performance. To demonstrate this approach, TiO_2 thin films with varying degrees of crystallinity were fabricated using atomic layer deposition (ALD). Etching rates were quantitatively evaluated across different pH environments (acidic, alkaline, and near-neutral) under both dark and illuminated conditions, including simulated sunlight and UV exposure. The results reveal that higher crystallinity significantly enhances corrosion resistance, and that initial film thickness also influences the degradation rate. These findings emphasize the utility of PEC *operando*-SE as a powerful diagnostic platform for guiding the design of more durable photoelectrochemical materials and systems.

Results and discussion

Operando-SE cell setup and TiO_2 as model system

To implement *operando*-SE, we utilized a customized PEC cell, as shown in Fig. 1 and SI Fig. S1 and S2. The cell includes an optical window through which light is introduced *via* a UV-resistant fiber optic cable. This setup allows direct light illumination on the photoelectrode and, at the same time, allows for real-time monitoring of corrosion-induced thickness changes using *operando*-SE (Fig. 1).

To demonstrate that the *operando*-SE system can be used to probe corrosion mechanisms, we first considered appropriate model photoelectrode materials and choose TiO_2 thin films; one of the most widely studied materials for use both as a photoelectrode and as a protective layer.[13,31–34] TiO_2 films were deposited on highly doped n++ silicon substrates using ALD under precisely controlled conditions, producing two representative polymorphs: amorphous TiO_2 (a-TiO_2) and fully crystalline TiO_2 (c-TiO_2). Details on the ALD process and deposition conditions are provided in the methods section and in the SI (Fig. S3). Surface morphological differences arising from

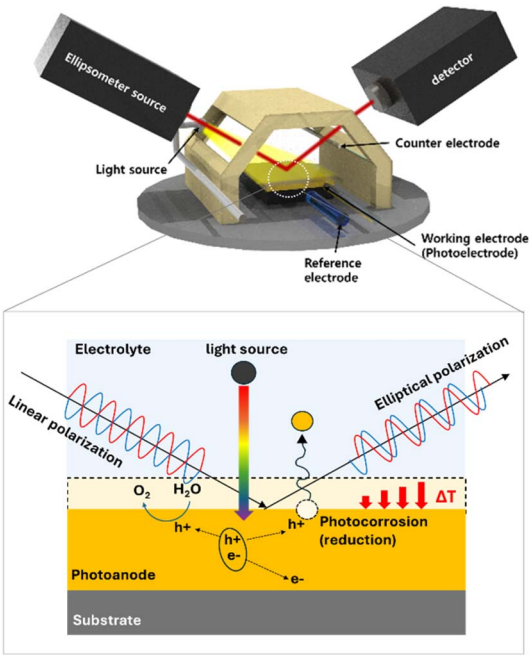

Fig. 1 Schematic diagrams illustrating the configuration for *operando* SE with a PEC system, and the real-time monitoring of photoelectrode corrosion within the PEC cell.

crystallinity are presented in Fig. S4, and optical band gaps extracted from UV-vis measurements are shown in Fig. S5.

We also carried out structural and chemical characterization of the as-deposited TiO_2 samples using grazing incidence X-ray diffraction (GIXRD), Raman spectroscopy, and AFM (Fig. 2). In the XRD patterns, no diffraction peaks were observed for the a-TiO_2, while the c-TiO_2 exhibited well-defined diffraction peaks, confirming its crystallinity (Fig. 2a). Raman spectra further supported these findings, with intensity variations of the characteristic peaks depending on the crystallinity (Fig. 2b). The c-TiO_2 showed anatase-phase Raman bands corresponding to Ti–O stretching vibrations (517 cm^{-1}, A_{1g}, B_{1g}; 642 cm^{-1}, E_g) and O–Ti–O bending vibrations (148 cm^{-1}, E_g; 201 cm^{-1}, E_g; 399 cm^{-1}, B_{1g}).[35–37] No Raman bands associated with rutile or brookite phases were observed.

AFM images revealed distinct differences in surface morphology depending on the crystallinity of the films, in agreement with previous reports[38,39] (Fig. 2c). While a-TiO_2 exhibited an amorphous surface without visible grains, c-TiO_2 displayed densely packed crystallites covering the entire surface, with no remaining amorphous regions. These results confirm that, through precise control of the ALD deposition parameters, we successfully fabricated TiO_2 thin films with well-defined and distinct crystallinity.

PEC behavior and corrosion resistance of TiO_2 films

Before analyzing the corrosion behavior of model photoelectrodes using *operando*-SE, we first evaluated their PEC response and corrosion resistance. The PEC response of the model samples was evaluated by potential-time (*V–t*) and current density-potential (*J–V*) characterization under chopped-illumination, as well as EIS (Fig. 3). The *V–t* shows the open circuit potential (OCP) under both dark and illuminated conditions. We observed an increase in OCP a-TiO_2 > c-TiO_2

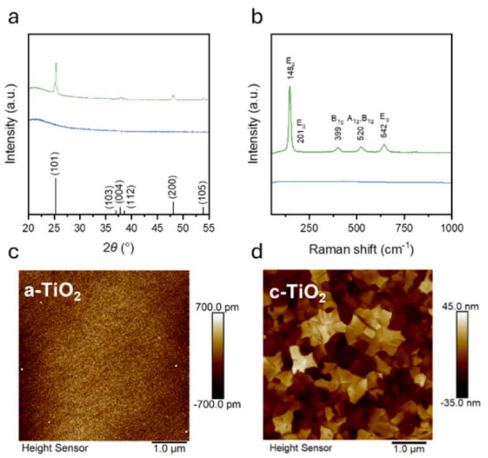

Fig. 2 (a) XRD patterns of both TiO_2 thin films grown by ALD on fused silica. The black lines show the diffraction peaks matched with ICDD reference data for the tetragonal crystal structure of the anatase polymorph of TiO_2 (PDF 00-021-1272). (b) Raman spectra of both TiO_2 thin films on fused silica. (c) AFM topography scans of the a-TiO_2 and c-TiO_2 grown on silicon.

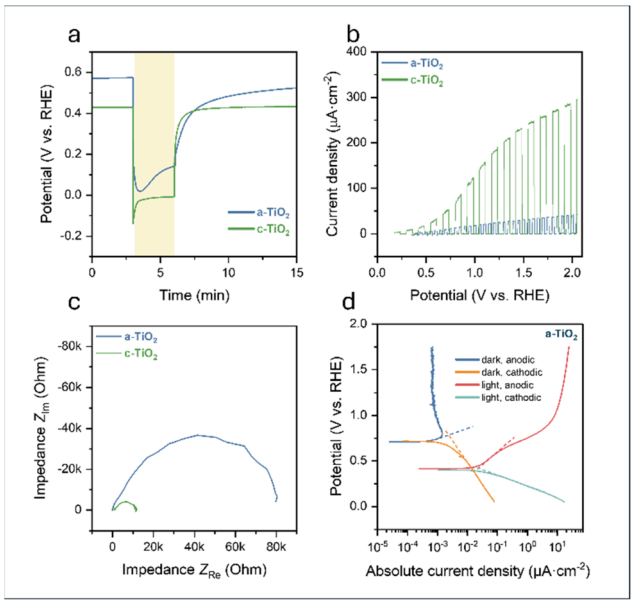

Fig. 3 (a) *V–t* (at open circuit) and (b) *J–V* characteristics of TiO_2 thin films, measured in phosphate buffer solution (pH 6). The yellow-shaded region in the *V–t* plot indicates illumination under 1 sun. (c) Nyquist plots of TiO_2 films acquired under 1 sun illumination at an applied potential of 1.23 V *vs.* RHE in phosphate buffer (pH 6). (d) LPR measurements for a-TiO_2 performed in 0.5 M H_2SO_4, using a scan rate of 2 mV s^{-1}; corrosion resistance was estimated *via* Tafel slope extrapolation.

(Fig. 3a). The photovoltage, derived from the difference between dark and illuminated OCP, exhibited transient behavior, which can be attributed to capacitive charging and discharging of defect states and surface trap states when the light is turned on or off.[40,41] In the case of c-TiO_2, the transition between dark and illuminated OCP became sharper, and the OCP reached a stable value more quickly. These trends suggest enhanced charge carrier transport in films with higher crystallinity, consistent with improved long-range structural order and reduced defect density.

Fig. 3b shows the *J–V* characteristics obtained from chopped light. The a-TiO_2 showed a photocurrent density of approximately 40 μA cm^{-2} at 2 V *vs.* RHE. In contrast, the c-TiO_2 exhibit photocurrent densities in the range of 300–360 μA cm^{-2} at the same potential, with a more negative onset potential. According to the EIS results, this trend can be attributed to improved charge-transfer kinetics at the surface with enhancing crystallinity, as evidenced by the decreasing semicircle diameter in the Nyquist plots (Fig. 3c).

To evaluate the corrosion resistance of the a-TiO_2, we carried out linear polarization resistance (LPR) measurements in both anodic and cathodic directions, as a representative sample in 0.5 M sulfuric acid (Fig. 3d). The polarization resistance was determined by extrapolating the linear regions of the anodic and cathodic branches of the Tafel plots obtained from the LPR measurements (see Methods section), and calculating the slope at the corrosion potential. The extracted value in the dark was approximately 26.1 MΩ cm^2, which is nearly 20 times higher

than the value measured under illumination 1.48 MΩ cm^2. This significant difference suggests a substantial decrease in corrosion resistance under light exposure, indicating the pronounced vulnerability of the a-TiO_2 film to photo-induced degradation. However, because photocurrent contributions under illumination play a significant role, LPR alone does not fully capture photocorrosion effects. Therefore, *operando*-SE provides a more direct and quantitative approach for their assessment.

PEC *Operando*-SE analysis with stability test

To verify the physical degradation of the photoelectrodes under illumination, *operando*-SE was applied under PEC operating conditions with continuous light irradiation (Fig. 4). The chronoamperometric responses of c-TiO_2 in sulfuric acid and those of a-TiO_2 in electrolytes with different pH values are provided in the SI (Fig. S6). Fig. 4a shows the changes in film thickness for a-TiO_2 and c-TiO_2 thin films, each exposed to 0.5 M sulfuric acid for up to 24 hours (h) under an applied potential of 1.23 V *vs.* RHE. Detailed experimental conditions and fitting procedures for the *operando*-SE measurements are provided in the SI (Fig. S7). The thickness of both TiO_2 layers was found to decrease linearly with time. The etch rate was extracted from the slope obtained by linear fitting of the plots of thickness *vs.* time.

For the a-TiO_2 model sample, the etch rate in the dark was 0.092 nm h^{-1}, which significantly increased under 1 sun illumination to 1.36 nm h^{-1}. In contrast, the c-TiO_2 sample exhibits negligible degradation during the 24 h chronoamperometric measurements, with etch rates of 0.01 nm h^{-1} under 1 sun illumination and 0.002 nm h^{-1} in the dark, respectively. These findings clearly indicate that the crystallinity of TiO_2 plays a crucial role in determining its corrosion resistance, and further highlight the capability of *operando*-SE to sensitively distinguish different corrosion behaviors depending on film crystallinity.

Motivated by this capability, we further applied PEC *operando*-SE to gain a deeper understanding of the corrosion dynamics of a-TiO_2 depending on the thickness, which exhibits significantly lower corrosion resistance, particularly under illumination (Fig. 4b). To extend these insights, we next examined the effect of electrolyte pH on corrosion behavior using PEC *operando*-SE. Although TiO_2 is generally regarded as stable over a wide pH range and its corrosion mechanisms are well documented,[42–44] quantitative analyses of the extent of degradation under operating conditions remain limited. Our *operando*-SE measurements provide such direct quantification. In pH 6 phosphate buffer, only minor etching was observed (Fig. 4c), and no significant photocorrosion was detected. Under strongly alkaline conditions, the a-TiO_2 film also remained comparatively stable, but gradual degradation was still discernible. At pH 14 (1 M NaOH), pronounced initial non-linearity was observed in all degradation curves regardless of illumination, followed by a transition to a linear regime after a few hours, with etch rates between 0.05 and 0.11 nm h^{-1} (Fig. 4d). The comparatively higher stability of TiO_2 under alkaline conditions may be related to surface chemical processes, whereby photohole-induced dissolution can be accompanied by redeposition of an amorphous titanium-containing layer that subsequently slows further degradation.[45]

At near-neutral and basic pH, the corrosion rate remains below 1 nm h^{-1} and is only weakly influenced by illumination. In contrast, in acidic media the corrosion rate exceeds 1 nm h^{-1} and reaches up to 1.7 nm h^{-1} under illumination, indicating a pronounced light-induced acceleration. This trend is consistent with the photocurrent data (Fig. S6), where higher currents are observed in acidic electrolyte, suggesting that corrosion contributes significantly to the measured current under these conditions. While comparison of AFM images acquired after prolonged chronoamperometry measurements (Fig. S8a) with pre-measurement images (Fig. 2) indicates morphological evolution for both a-TiO_2 and c-TiO_2, surface topography alone does not allow reliable discrimination of phase-dependent corrosion susceptibility. In contrast, *operando*-SE measurements quantitatively demonstrate greater material loss for a-TiO_2, confirming that the amorphous phase is intrinsically more susceptible to acid-induced corrosion. Collectively, these findings highlight the value of *operando*-SE as a quantitative benchmark for stability assessment across the entire pH range.

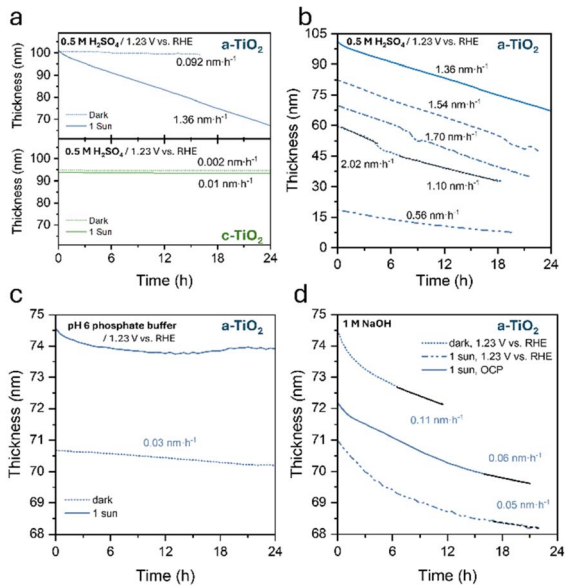

Fig. 4 *Operando*-SE thickness measurements and corresponding etch rates of a-TiO_2 films on n++ Si under different electrolyte conditions: (a) strongly acidic solution, (b) films with varying initial thickness, (c) pH 6 phosphate buffer, and (d) 1 M NaOH. Measurements were performed at 1.23 V *vs.* RHE or at OCP, both in the dark and under 1 sun illumination.

PEC *Operando*-SE analysis with stability test and charge dynamics

In continuation of our prior examination of corrosion of photoanode *via operando*-SE, we combined *operando*-SE with EIS to gain deeper mechanistic insight into photocorrosion. This integrated approach enables concurrent tracking of physical and electrochemical dynamics, providing a more

comprehensive view of degradation processes. EIS measurements were continuously performed on an a-TiO_2 sample in 0.5 M H_2SO_4, under a constant dc bias potential of 1.23 V *vs.* RHE (Fig. 5, Nyquist and Bode plots are shown in Fig. S9a–d). An equivalent circuit model with two time-constants (Fig. 5e) was used to fit the experimental data for the impedance behavior of the semiconductor electrolyte interface.[46–48] The extracted values for the model parameters are plotted in Fig. 5, compared with the thickness changes concurrently measured by *operando*-SE.

The high-frequency resistance (R_{SC}), which reflects charge transport through the bulk of the film and across the space-charge layer,[46] was lower under illumination than in the dark, because of the higher density of photogenerated carriers in illuminated films (Fig. 5a). Although photocorrosion was approximately 10 times faster under illumination than in the dark, the trend in R_{SC} remained similar in both cases. This indicates that photocorrosion is independent of bulk charge-transport resistance and instead originates predominantly at the surface–electrolyte interface.

Interestingly, the charge transfer resistance (R_{CT}) continued to increase over several hours under illumination before reaching a steady state, whereas in the dark, it continued to rise over the entire duration of the measurement (Fig. 5b). Despite this behavior, the total etching depth after 24 hours in the dark was only a few nanometers, which is comparable to the corrosion observed within the first two hours under illumination.

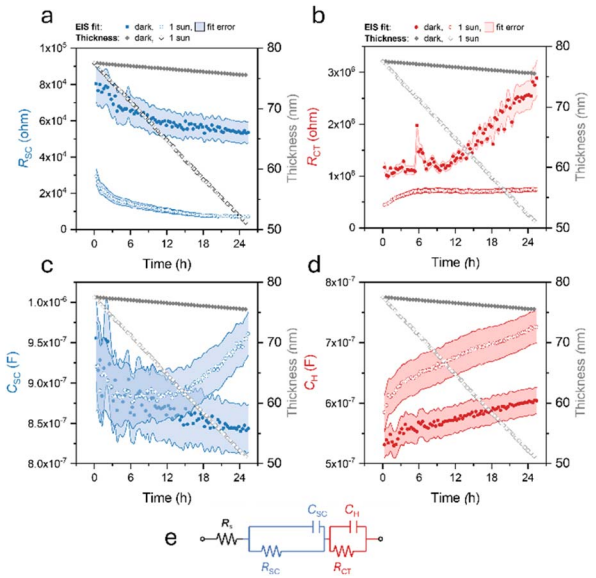

Fig. 5 Fitting parameters for consecutive EIS spectra on a sample of a-TiO_2 under PEC operating conditions. Shown are the parameters (a) R_{SC}, (b) R_{CT}, (c) C_{SC}, and (d) C_H corresponding to (e) the equivalent circuit, as functions of time. The corresponding film thickness as a function of time, determined independently by *operando*-SE, is overlaid in each panel as a grey trace. Filled symbols represent dark conditions, and open symbols represent illumination under 1 sun. All measurements were conducted at 1.23 V *vs.* RHE with a 25 mV AC perturbation over the frequency range of 1 MHz to 0.1 Hz. (See Fig. S9 for raw data and further details on the equivalent circuit).

The increase in R_{CT} during both the initial 6 hours under illumination and 24 h under dark may reflect changes in charge transfer between electrolyte and photoelectrode as corrosion progresses. Notably, although corrosion-induced variations in R_{CT} were observed, the R_{CT} stabilized after a certain degree of degradation. This finding indicates that the charge transfer of the photoelectrode surface can remain relatively stable although photocorrosion remains during continuous operation.

The capacitance of the Helmholtz layer (C_H) shows a slight increase during the degradation experiment, both with and without illumination (Fig. 5c). This increase may be associated with a modest increase in surface roughness as the film is gradually etched.

Under illumination, a more notable increase in the space charge region capacitance (C_{SC}) was observed after approximately 15 hours of operation, particularly when the residual TiO_2 film thickness dropped below ~60 nm (Fig. 5d). This behavior may be attributed to a reduced flux of photogenerated holes in the thinner films, resulting from lower photon absorption and reduced charge-carrier separation efficiency, as the depletion width becomes limited by the decreasing film thickness. This transition correlates with the decreasing photocorrosion rates observed for films thinner than 50 nm, as shown in Fig. 4b.

Through this combined analysis, we were able to directly verify the progression of photocorrosion in TiO_2-based photoelectrodes which is one of the most widely used materials in PEC system and confirm that this *operando*-SE approach, when integrated with complementary techniques, provides valuable insights into PEC dynamic degradation behaviour, and holds strong potential as a synergistic tool for future studies.

Summary

In this study, we demonstrated *operando*-SE as a precise and effective technique for real-time monitoring of photocorrosion in photoelectrodes under realistic PEC conditions. To enable systematic analysis, TiO_2 thin films with tuned crystallinity (amorphous, mixed-phase, and fully crystalline) were fabricated using ALD. *Operando*-SE allowed continuous and quantitative tracking of surface degradation over 18–24 hours across different electrolyte environments, including 0.5 M sulfuric acid, 1 M sodium hydroxide, and a pH 6 phosphate buffer, under both dark and illuminated conditions (1 sun and 365 nm LED). The results revealed that degradation behavior is highly dependent on crystallinity, illumination, and pH. For instance, amorphous TiO_2 films showed pronounced etching in acidic media under illumination, with etch rates reaching up to 1.33 nm h^{-1}, whereas fully crystalline films exhibited markedly enhanced stability, with etch rates as low as 0.01 nm h^{-1}. Further insights were obtained by combining *operando*-SE with EIS, which confirmed that photocorrosion predominantly occurs at the surface and is closely associated with interfacial charge transport dynamics. This integrated approach provides a comprehensive understanding of time-resolved degradation mechanisms and offers a practical strategy for enhancing the

long-term durability of PEC electrodes and other photoelectrocatalytic materials.

Methods

Preparation for TiO_2 film

Crystalline, single-side polished, 2 × 2 cm^2, arsenic-doped Si wafer pieces (n++ Si(100), thickness 525 μm, ρ < 0.005 Ω cm, Siegert Wafer) and fused silica, 2 × 2 cm^2, wafer pieces (quartz, thickness 500 μm, Siegert Wafer) were used as substrates.

Substrates were cleaned using ultrasonication with successive baths of absolute ethanol (99.99%, Sigma-Aldrich) and deionized water (DI H_2O, ρ > 18 MΩ cm, Millipore Direct-Q). To remove the native silicon oxide layer from the silicon wafer pieces, they were held in a buffered oxide etchant (BOE, 6 : 1 NH_4F : HF, Sigma-Aldrich) for 1 min, then rinsed with DI water and dried with a nitrogen stream (99.999%, Linde).

A Picosun R-200 Advanced ALD system was used to deposit TiO_2 thin films at various temperatures between 180 °C and 280 °C. Deposition at 180 °C yields a-TiO_2, whereas deposition at ≥260 °C results in crystalline c-TiO_2. Intermediate deposition temperatures produce mixed-phase films, consisting of TiO_2 crystallites dispersed within an amorphous TiO_2 matrix. The samples were used as deposited, without any post-synthetic treatment. Both precursors titanium tetrachloride ($TiCl_4$, electronic-grade, Dockweiler Chemicals) and DI H_2O were maintained in stainless steel vessels at 22 °C and used without further purification. Nitrogen (N_2, 99.9999%, Linde) was used as both inert carrier and purge gas with a flow rate of 80 sccm (standard cubic centimeters per minute). The pressure inside the ALD chamber during thermal deposition was 5 mbar. An optimized TiO_2 ALD cycle consisted of the injection of $TiCl_4$ for 0.1s, a N_2 purging step for 4.9 s, the injection of H_2O for 0.1s and a N_2 purging step for 13.4 s with a growth rate of 0.50–0.65 Å per cycle (SI Fig. 1). For demonstration of the *operando* ellipsometry method, samples grown at 180 °C and 260 °C were chosen as model systems. The crystalline samples were obtained with 2000 ALD cycles. For the amorphous samples, different film thicknesses were obtained by varying the number of cycles.

The synthesis parameters were chosen after reactor-specific optimization of the ALD process for TiO_2 growth was carried out, to obtain the characteristic growth per cycle within the ALD process temperature window (SI Fig. 1). The homogeneity of the thermally ALD-grown TiO_2 thin film on n++ Si 4″ wafer was verified by *ex-situ* SE thickness mapping using an automated sample translation stage (SI Fig. 5). It is assumed that crystallization of amorphous ALD-grown TiO_2 below a critical thickness of about 10 nm does not occur due to the high internal strain in the layer.[8,49]

Characterization

Film thickness and optical constants were measured by *ex-situ* and *operando*-SE using a RC2 spectroscopic ellipsometer (J.A. Woollam). The *ex-situ* SE measurements in reflection mode were performed at angles of incidence of 60–70°, with wavelengths in the range of 210–2500 nm. The SE data were fitted with a Tauc–Lorentz oscillator model (SI Fig. 2) using the CompleteEASE software (J.A. Woollam).

The phase of the TiO_2 thin films was characterized by GIXRD at room temperature with a D8 DISCOVER diffractometer (Bruker) under a grazing incidence angle of 1.0° and Cu K-α radiation. Raman spectroscopy was used to verify the phase of the as-grown thin films with an alpha300 R confocal Raman microscope (WITec) using laser excitation wavelengths of 532 nm and 633 nm, at a power of 15 mW. The Raman scattered light was analyzed in a spectrometer with a diffraction grating with 600 g mm^{-1} (grooves per mm) and a Peltier-cooled charge coupled device detector.

High-resolution topography images were acquired using a Dimension Icon AFM (Bruker). PEAKFORCE-HIRS-SSB probes (Bruker) with a nominal tip radius of 1 nm, a spring constant of 0.12 N m^{-1} and a resonance frequency of 110 kHz were used for measurements in air. Low peak velocities of 0.665–6.65 μm s^{-1} and low peak forces of 350–500 pN were used. By flattening the AFM images with a line-by-line least-squares polynomial fit, the background tilt on each line was removed.

The PEC characterization of thermally ALD-grown TiO_2 thin films on n++ Si was performed using a VersaSTAT4 potentiostat (Princeton Applied Research – AMETEK), which was connected to a three-electrode photoelectrochemical cell (PECC-2, Zahner-Elektrik) with a quartz window for illumination, a coiled platinum wire as the counter electrode, an Ag/AgCl reference electrode (RE-1B, 3 M NaCl, $E^0_{Ag/AgCl}$ = 195 mV *vs.* RHE, ALS) and the sample under study as the working electrode. For *i–V* curves, three cyclic voltammetry cycles were recorded at a scan rate of 25 mV s^{-1}, and the most stable cycle is selected.

For LPR measurements, four potential scans were carried out, starting at OCP, and scanning in anodic and in cathodic directions, in the dark and under illumination, each time allowing for OCP to stabilize. In all cases the scan rate was 2 mV s^{-1}. The polarization resistance was obtained from the Stern–Geary equation:

$$R_p = \frac{\beta_a \beta_c}{2.303\, I_{corr}(\beta_a + \beta_c)}$$

where β_a and β_c are the slopes (Tafel constants) of the linear regions of the anodic and cathodic branches respectively, and the I_{corr} is the corrosion current (obtained at the intersection of the Tafel extrapolations). We note that, under illumination, the measured current may include contributions from photocurrent associated with interfacial charge-transfer reactions, and LPR alone cannot unambiguously distinguish between photocurrent generation and photocorrosion processes.

Operando-SE technique

For the *operando*-SE investigations, the samples were placed in an *in-situ* PEC (J.A. Woollam) with a platinum grid as counter electrode and a platinum pseudo-reference electrode. 0.5 M sulfuric acid (Carl Roth), 1 M NaOH (Merck) and phosphate buffer (pH 6, 0.09 M KH_2PO_4, 0.01 M NaOH, 0.5 M K_2SO_4, Sigma-Aldrich), were used as acidic, alkaline and neutral electrolytes, respectively. The electrolyte was purged with argon

(99.999%, Linde) for 15 min before use to remove dissolved oxygen. The samples were illuminated from the front with simulated solar light (AM 1.5 G, 100 mW cm^{-2}) using a solar simulator (Model LS0306, 300 W, LOT-QuantumDesign) or with UV light using a 365 nm fiber-coupled LED (Thorlabs, M365FP1, 1.4 A) with a fixed incidence angle of 70° (SI Fig. 2–4). EIS at 1.23 V *vs.* RHE with an amplitude perturbation of 25 mV in the frequency range from 1 MHz to 0.1 Hz was used to measure the interfacial charge transfer resistance. The EIS data were fitted using the ZView 4 software (Scribner Associates).

Author contributions

F. M. T. conceived the idea. M. S. and F. M. T. designed the research. M. S., S. S., T. K., and F. M. T supervised the project. J. K. and M. S. synthesized the TiO_2 coatings by ALD, determined the film thickness by SE and the atomic structure by XRD and Raman spectroscopy, conducted PEC measurements, and analyzed the data. R. R. performed AFM experiments. M. S., F. M. T., S. S. and J. K. analyzed the data and wrote the manuscript. All authors have given approval to the final version of the manuscript.

Conflicts of interest

There are no conflicts to declare.

Data availability

The data that support the findings of this study are openly available in Zenodo at https://doi.org/10.5281/zenodo.17076397.

Supplementary information (SI) is available. See DOI: https://doi.org/10.1039/d5el00179j.

Acknowledgements

The authors thank Dr Steffen Fengler for insightful scientific discussions. The authors gratefully acknowledge Manuela Keller for her assistance with the supplemental AFM characterization of the samples post-degradation. The authors acknowledge support from the Helmholtz Association through program-oriented funding (POF IV). F. M. T. acknowledges support from the "Helmholtz Distinguished Professorship" program of the Helmholtz Association. Part of this work (inception of the idea and design of the photoelectrochemical *operando* cell) was conducted through support of the Liquid Sunlight Alliance (LiSA), which is supported by the U.S. Department of Energy, Office of Science, Office of Basic Energy Sciences, Fuels from Sunlight Hub under Award Number DE-SC0021266.

References

1 D. Li, K. Yang, J. Lian, J. Yan and S. Liu, *Adv. Energy Mater.*, 2022, **12**, 2201070.
2 V. Kumaravel, J. Bartlett and S. C. Pillai, *ACS Energy Lett.*, 2020, **5**, 486–519.
3 H. Song, S. Luo, H. Huang, B. Deng and J. Ye, *ACS Energy Lett.*, 2022, **7**, 1043–1065.
4 M. G. Walter, E. L. Warren, J. R. McKone, S. W. Boettcher, Q. Mi, E. A. Santori and N. S. Lewis, *Chem. Rev.*, 2010, **110**, 6446–6473.
5 L.-J. Guo, J.-W. Luo, T. He, S.-H. Wei and S.-S. Li, *Phys. Rev. Appl.*, 2018, **10**, 064059.
6 M. R. Shaner, S. Hu, K. Sun and N. S. Lewis, *Energy Environ. Sci.*, 2014, **8**, 203–207.
7 E. A. Miller and G. L. Richmond, *J. Phys. Chem. B*, 1997, **101**, 2669–2677.
8 A. Paracchino, N. Mathews, T. Hisatomi, M. Stefik, S. D. Tilley and M. Grätzel, *Energy Environ. Sci.*, 2012, **5**, 8673–8681.
9 S. Zhang, I. Ahmet, S.-H. Kim, O. Kasian, A. M. Mingers, P. Schnell, M. Kölbach, J. Lim, A. Fischer, K. J. J. Mayrhofer, S. Cherevko, B. Gault, R. van de Krol and C. Scheu, *ACS Appl. Energy Mater.*, 2020, **3**, 9523–9527.
10 S. Vanka, G. Zeng, T. G. Deutsch, F. M. Toma and Z. Mi, *Front. Energy Res.*, 2022, **10**, 840140.
11 F. Nandjou and S. Haussener, *J. Phys. D: Appl. Phys.*, 2017, **50**, 124002.
12 S. Hu, N. S. Lewis, J. W. Ager, J. Yang, J. R. McKone and N. C. Strandwitz, *J. Phys. Chem. C*, 2015, **119**, 24201–24228.
13 S. Hu, M. R. Shaner, J. A. Beardslee, M. Lichterman, B. S. Brunschwig and N. S. Lewis, *Science*, 2014, **344**, 1005–1009.
14 H. Gerischer, *J. Electroanal. Chem. Interfacial Electrochem.*, 1977, **82**, 133–143.
15 S. Chen and L.-W. Wang, *Chem. Mater.*, 2012, **24**, 3659–3666.
16 K. Jenewein, A. Kormanyos, J. Knöppel, K. J. J. Mayrhofer and S. Cherevko, *ECS Meet. Abstr.*, 2022, 1886.
17 H. Tomáš, K. Peter, R. Miquel Gamón, M. Vladimír and M. Iva, *Int. J. Hydrogen Energy*, 2024, **57**, 187–197.
18 M. Rudak, H. Saleem, H. Park and Y. Park, *ACS Appl. Energy Mater.*, 2025, **8**, 9473–9481.
19 A. Tsyganok, P. Ghigna, A. Minguzzi, A. Naldoni, V. Murzin, W. Caliebe, A. Rothschild and D. S. Ellis, *Langmuir*, 2020, **36**, 11564–11572.
20 F. Paparoni, G. Alizon, A. Zitolo, S. J. Rezvani, A. Di Cicco, H. Magnan and E. Fonda, *Phys. Chem. Chem. Phys.*, 2024, **26**, 3897–3906.
21 J. Shi, X. Zhao and C. Li, *Catalysts*, 2023, **13**(2), 217.
22 G. Zeng, T. A. Pham, S. Vanka, G. Liu, C. Song, J. K. Cooper, Z. Mi, T. Ogitsu and F. M. Toma, *Nat. Mater.*, 2021, **20**, 1130–1135.
23 W. Yu, H. J. Fu, T. Mueller, B. S. Brunschwig and N. S. Lewis, *J. Chem. Phys.*, 2020, **153**, 20902.
24 H. Fujiwara, *Spectroscopic Ellipsometry: Principles and Applications*, Wiley, Chichester, England, Hoboken, NJ, 2007.
25 J. N. Hilfiker, N. Singh, T. Tiwald, D. Convey, S. M. Smith, J. H. Baker and H. G. Tompkins, *Thin Solid Films*, 2008, **516**, 7979–7989.
26 M. Losurdo, M. Bergmair, G. Bruno, D. Cattelan, C. Cobet, A. de Martino, K. Fleischer, Z. Dohcevic-Mitrovic, N. Esser,

M. Galliet, R. Gajic, D. Hemzal, K. Hingerl, J. Humlicek, R. Ossikovski, Z. V. Popovic and O. Saxl, *J. Nanopart. Res.*, 2009, **11**, 1521–1554.
27 T. Ohtsuka, M. Masuda and N. Sato, *J. Electrochem. Soc.*, 1985, **132**, 787–792.
28 T. Van Schaftinghen, S. Joiret, C. Deslouis and H. Terryn, *J. Phys. Chem. C*, 2007, **111**, 14400–14409.
29 D. Ngo, H. Liu, N. Sheth, R. Lopez-Hallman, N. J. Podraza, M. Collin, S. Gin and S. H. Kim, *npj Mater. Degrad.*, 2018, **2**, 1–9.
30 T. C. Kaspar, J. T. Reiser, J. V. Ryan and N. A. Wall, *J. Non-Cryst. Solids*, 2018, **481**, 260–266.
31 B. Mei, T. Pedersen, P. Malacrida, D. Bae, R. Frydendal, O. Hansen, P. C. K. Vesborg, B. Seger and I. Chorkendorff, *J. Phys. Chem. C*, 2015, **119**, 15019–15027.
32 X. Shen, R. Yanagi, D. Solanki, H. Su, Z. Li, C.-X. Xiang and S. Hu, *Front. Energy Res.*, 2022, **9**, 799776.
33 M. Hannula, H. Ali-Löytty, K. Lahtonen, E. Sarlin, J. Saari and M. Valden, *Chem. Mater.*, 2018, **30**, 1199–1208.
34 J. Saari, H. Ali-Löytty, M. Honkanen, A. Tukiainen, K. Lahtonen and M. Valden, *ACS Omega*, 2021, **6**, 27501–27509.
35 W. F. Zhang, Y. L. He, M. S. Zhang, Z. Yin and Q. Chen, *J. Phys. D: Appl. Phys.*, 2000, **33**, 912–916.
36 A. Niilisk, M. Moppel, M. Pärs, I. Sildos, T. Jantson, T. Avarmaa, R. Jaaniso and J. Aarik, *Cent. Eur. J. Phys.*, 2006, **4**, 105–116.
37 F. Li and Y. Gu, *Mater. Sci. Semicond. Process.*, 2012, **15**, 11–14.
38 M. Kaipio, T. Blanquart, Y. Tomczak, J. Niinistö, M. Gavagnin, V. Longo, H. D. Wanzenböck, V. R. Pallem, C. Dussarrat, E. Puukilainen, M. Ritala and M. Leskelä, *Langmuir*, 2014, **30**, 7395–7404.
39 J.-P. Niemelä, G. Marin and M. Karppinen, *Semicond. Sci. Technol.*, 2017, **32**, 093005.
40 C. Ros, T. Andreu, M. D. Hernández-Alonso, G. Penelas-Pérez, J. Arbiol and J. R. Morante, *ACS Appl. Mater. Interfaces*, 2017, **9**, 17932–17941.
41 Z. Tang, L. Fang, N. Xu and R. Liu, *J. Appl. Phys.*, 2015, **118**, 185309.
42 A. Kafizas, Y. Ma, E. Pastor, S. R. Pendlebury, C. Mesa, L. Francàs, F. Le Formal, N. Noor, M. Ling, C. Sotelo-Vazquez, C. J. Carmalt, I. P. Parkin and J. R. Durrant, *ACS Catal.*, 2017, **7**, 4896–4903.
43 A. Imanishi, T. Okamura, N. Ohashi, R. Nakamura and Y. Nakato, *J. Am. Chem. Soc.*, 2007, **129**, 11569–11578.
44 T. Nakajima, T. Nakamura and T. Tsuchiya, *Catalysts*, 2019, **9**, 725.
45 Y. Yang, Y. Ling, G. Wang, T. Liu, F. Wang, T. Zhai, Y. Tong and Y. Li, *Nano Lett.*, 2015, **15**, 7051–7057.
46 F. L. Formal, N. Tétreault, M. Cornuz, T. Moehl, M. Grätzel and K. Sivula, *Chem. Sci.*, 2011, **2**, 737–743.
47 K. Sivula, F. Le Formal and M. Grätzel, *ChemSusChem*, 2011, **4**, 432–449.
48 L. Bertoluzzi, P. Lopez-Varo, J. A. J. Tejada and J. Bisquert, *J. Mater. Chem. A*, 2016, **4**, 2873–2879.
49 J. Aarik, A. Aidla, T. Uustare and V. Sammelselg, *J. Cryst. Growth*, 1995, **148**, 268–275.